Sensor and Simulation Notes

Note 403

December 1996

NUMERICAL ANALYSIS OF PLANAR BICONE ARRAYS

Daniel T. McGrath, LtCol, USAF

USAF Phillips Laboratory
Kirtland AFB, NM

ABSTRACT

A numerical model is used to investigate the radiating and receiving properties of planar bicone arrays for use as ultrawideband, time-delay scanned antennas. The approach employs a hybrid of the finite element method with periodic boundary conditions to compute the electric fields in a unit cell of the assumed-infinite array. It is observed that the input impedance of the structure at broadside scan is very near that of 60π Ohms predicted for a self-complementary array. It is shown that the useful bandwidth of the planar bicone array is restricted to those frequencies for which there are no visible grating lobes. At broadside scan (or incidence) the upper frequency limit is that at which the elements are spaced one wavelength apart. This paper discusses the numerical modeling approach, and computed results with two different feed region geometries.

PL 96-1202

1. INTRODUCTION

A variety of potentially interesting applications require focused radiation of high-power radio frequency (RF) transients. Two competing alternatives are: a single high-power source feeding a large aperture horn or reflector; and an array of small antennas individually fed by synchronized, medium-power sources.

An example of the first alternative is the reflector impulse radiating antenna (RIRA) [1]. Its experimental implementation used a large parabolic reflector fed by a transverse electromagnetic (TEM) horn joining the reflector edges to a single spark gap switch. Its large size (12' diameter) allowed a long "fill time," permitting the antenna to radiate frequencies lower than 40 MHz [2],[3].

However, the single-switch approach is not suitable for applications that require a repeatable waveform because spark gap switches suffer from "jitter," a pulse-to-pulse variation in the time at which they break relative to the charging pulse's leading edge. Solid-state switches, such as those using bulk avalanche in Gallium Arsenide (GaAs), on the other hand, generate more repeatable waveforms, because they are triggered by an illuminating laser source, not by self-breaking. This suggests that a large array of the medium-power solid state switches could radiate transients as well, or better, than a single-source antenna [4:25]. In addition, such an array would have the valuable capability for electronic scanning.

A problem related to switching arrays that has not been adequately addressed is that of the design of the radiating elements. The limitations that inter-element mutual coupling might impose on the scanning capabilities and the radiated spectral content is largely unknown.

This paper begins an exploration of these issues by considering a practical embodiment of the self-complementary array concept. It summarizes analyses performed using the periodic hybrid finite element method to calculate the fields in the vicinity of a receiving array of "planar bicone" elements, and the resulting received and reflected power. It shows that even with these nearly-ideal radiating elements, the frequency content of transmitted and received signals is essentially limited to below the frequency at which the array elements are one wavelength apart, and even lower if the array is to be electronically steered. On the positive side, the results show that the array's input impedance is fairly stable over the permissible frequency range, remaining within 25% of the theoretical value of 60π Ohms for a self-complementary antenna.

2

2. THE SELF-COMPLEMENTARY ARRAY CONCEPT

A self-complementary antenna is a planar metallic structure whose rotation by 90° about its feed point forms the "complementary" structure, with air replacing metal and vice versa. Deschamps [5] showed that such antennas have constant input impedance of $\eta_0/2$, where $\eta_0 = 120\pi$ Ohms is the impedance of free space. Figure 1 shows an array whose elements are planar bicones. In the case when $d_x = d_y$, the structure is self-complementary. Baum [6] derived the input impedance for general arrays of planar bicones. For a square lattice with $\lambda \gg d_x$, it is $\eta_0\cos(\theta)/2$ or $\eta_0\sec(\theta)/2$ for scanning in the E and H planes, respectively, while for $\lambda \ll d_x$, it is $\eta_0/2$. Hence, in theory, the frequency-independent properties of self-complementary antennas also extend to arrays. The computed results discussed below show that this is very nearly true even when a practical (non-point-source) feed is used.

Note that planar bicone arrays, when used as sources, radiate equally in two directions. That limitation is accepted for purposes of this paper. Later investigations will deal with directional elements such as TEM horns. The properties of the self-complementary array serve as a baseline that is optimum in terms of frequency response.

3. MODELING APPROACH

3.1. Computational Method

A general-purpose solution method was previously developed for calculating the reflection and transmission properties of planar periodic structures [7]. It uses the finite element method (FEM) in conjunction with periodic boundary conditions to compute the electric fields in a unit cell of the structure. For purposes of this work, a capability for modeling resistive wires was incorporated, as discussed in Appendix A. Although FEM is inherently a frequency domain method, it can be used for UWB studies by repeating the solution for a number of frequency points within the bandwidth of interest. The periodicity conditions allow the solution to be restricted to a single unit cell, but that means the results will only be valid for "large" arrays, typically ten or more elements across.

Figure 2 shows a practical realization of the self-complementary array that allows for feeds that are not ideal point sources. The sources might be placed directly across the gaps

between plates, or might feed the bicones by TEM transmission lines. The modeling approach considered this antenna in the receiving mode, with the sources represented by resistive wires whose resistance (assumed real) is the same as the source impedance.

The dashed lines in Figure 2 are the outline of a unit cell. The definition of the unit cell is not unique--this one was chosen so that the source points are within the perimeter. Figure 3 shows its representation for purposes of the FEM calculation: The unit cell is truncated at planes $\pm h$ above and below the metallic structure. The tetrahedral cells are a subdivision of the free space within that region. Figure 3 shows only the cells on the $-z$ side, with shading showing those cell faces associated with conductors, and thick lines indicating those edges where resistive wire boundary conditions are set. Periodicity conditions are imposed on the $\pm x$ and $\pm y$ unit cell faces, while periodic radiation conditions are imposed on the $\pm z$ faces.

The unit cell model is illuminated from the $-z$ side by a plane wave propagating at an arbitrary angle (θ_0, ϕ_0). The resulting electric field values on that face form the right hand side of a matrix equation. The matrix solution gives the electric field along every tetrahedron edge. The reflection and transmission into $-z$ and $+z$ half spaces are calculated from the field values at $z=-h$ and $z=+h$, respectively. The field values along the resistive wire edges give the power absorbed by the array.

3.2. Convergence Checks

There are two uncertainties associated with the hybrid FEM modeling: (1) the grid resolution of the physical structure; and (2) the number of Floquet modes used in representing the external radiation conditions. (Appendix B discusses the properties of Floquet modes.) To address the first issue, a second geometry model, shown in Figure 4, was created. Its maximum edge length is $\lambda_0/20$, one half that of the model in Figure 3. Table I shows the convergence of received power vs. the maximum Floquet mode index N_{max} for broadside incidence with each of the two mesh models. The total number of modes used is $2(2N_{max}+1)^2$, with the mode indices in both x and y directions including the range $[-N_{max}, N_{max}]$. For each combination there are both TE and TM modes. The results of Table I indicate that the low-resolution model of Figure 3 is adequate for calculations up to at least f_0 and that ± 5 Floquet modes in each direc-

tion is adequate. Under these conditions, the results for received current are within 1.5% of the converged result with the fine grid model. However, for frequencies near $2f_0$, the current calculation is in error by more than 5%, and the fine mesh model must be used. The number of Floquet modes required is inversely proportional to the mesh edge length in the radiation boundary, so a finer mesh requires correspondingly more modes. The calculations in this report used either the coarse mesh with ± 5 modes, or the fine mesh with ± 10 modes.

4. NUMERICAL RESULTS

4.1. Received Power vs. Frequency

Figure 5 shows the computed power absorbed by loads whose impedance is $\eta_0/2$, and scattered in the forward and reverse directions, when the array is illuminated at normal incidence. The received power is nearly constant at 50% up to f_0, but falls off dramatically above that frequency. At all frequencies, the sum of forward and back scatter is 50%.

For frequencies below f_0, there is only one propagating Floquet mode (radiating lobe) in each direction, normal to the array. The impedance of that mode is η_0. The incident field excites currents on the bicones, which then "see" three impedances in parallel: $\eta_0/2$ for the load resistor; and η_0 for each propagating mode. Hence, it is expected that under ideal conditions one half of the power will be absorbed by the loads, and the other half will reradiate, an equal part in each direction. This is exactly the case in the low frequency limit, but at higher frequencies the non-ideal sources cause a slight difference between the forward and back scatter. Section 4.3 will show in some detail how the feed region geometry affects the division of power, but in general, the shape of the received power vs. frequency is relatively insensitive to the feed design.

As frequency increases through f_0, more than one Floquet mode can propagate in each direction. In fact, with the square lattice, a total of 16 higher order modes can exist when $f_0 < f < \sqrt{2}f_0$, 8 directed into each half space. Their directions of propagation are in the cardinal planes, a pair of modes TE and TM to z. The impact they have is that now the currents on the bicones can, and do, reradiate in those other directions. It is not simply the relative impedance of those other modes vs. that of the load that determines how much power goes into each, but

also the shape of the current distribution on the plates. The fact that the received power goes so suddenly to nearly zero above f_0 indicates that mutual coupling causes the current distribution to assume a form that results in no current flow through the loads, such as equal and opposite currents on each side of the feed gap.

The solid line in Figure 5 may be regarded as the impulse response magnitude for broadside scan. Figure 6 is the corresponding phase, which has been linearized to re-reference the coordinate origin to the center of the load. The nonlinear phase characteristic near and above f_0 indicates that waveforms containing those frequencies would not be radiated or received intact, but would suffer distortion due to dispersion.

4.2. Input Impedance

The input impedance that a transmitting source would see was found as the ratio of open circuit voltage to short circuit current. For each frequency, the impedance load was replaced, alternately, by a conducting wire (short circuit) and a very high resistance (an effective open circuit).

Figure 7 shows the calculated resistance and reactance as a function of frequency. The resistance is very nearly $\eta_0/2$ for all frequencies except those near the onset of grating lobes at f_0 and $\sqrt{2}f_0$. In the usable frequency range $(0, f_0)$, the input resistance is stable and the reactance is nearly zero. This implies that a transmitting source or receiving circuit can be impedance matched over wide bandwidths without tuning, which is a necessary property for radiating or receiving transients.

4.3. Alternate Feed Region Geometry

Figure 8a shows a closeup of the feed region used for the previous calculations. Figure 8b is an alternate geometry that more closely approximates a point source feed.

Calculations for the received and scattered power for the new geometry are shown in Figure 9. The received power is substantially the same as in Figure 5, but the fractional forward and back scatter are different. This justifies the earlier statement that the percentages of scattered power differ from the expected 25% due to the non-ideal feed geometry. The phase

6

of the received current was identical to that of the original geometry, shown in Figure 6.

Figure 10 shows the computed input impedance with the new feed geometry. In comparison to Figure 7, it is noteworthy that the resistance is still closer to $\eta_0/2$ in the range $(0, f_0)$ and the reactance is more nearly constant. These are indications that the feed geometry in Figure 8b can provide a better broadband impedance match to a transient source.

4.4. Scanning Effects

A transmitting ultrawideband array can be electronically scanned by adjusting the timing sequence of its individual sources. However, the spectral content of the radiated pulse will not generally be the same, due to the possibility of grating lobe effects. For wideband signals there is, strictly speaking, no such thing as a grating lobe. Instead, energy from a transmitted pulse that does not propagate in the main beam direction will be spread out in angle, with the lower frequencies radiating nearly along the array surface, and progressively higher frequencies radiating progressively nearer to broadside.

The performance of the planar bicone array for an oblique-incidence wave is illustrated by Figures 11 and 12. They show, again for the receiving case, the power absorbed by an $\eta_0/2$ load, and its phase, respectively, for an incident wave arriving from 30° off normal. Results are shown for both the H plane and E plane, which represent, respectively, scanning in the x-z and y-z planes, for a y-polarized source. The received power drops abruptly just past $.65 f_0$ due to the onset of the grating lobe. At that frequency, the phase has a slight discontinuity, but continues on fairly linearly up to f_0 , where it drops steeply, just as it did for broadside incidence.

Figures 13 and 14 are computed results for an incident wave arriving from 60° off normal. The bandwidth is, as expected, even more limited, with the rolloff near $.5 f_0$. In addition, the low frequency limit on received power is not 50%, but somewhat less than 45%. This is due to the fact that the modal impedance for the dominant Floquet mode (the incident field) varies as $\cos(\theta_0)$ or $\sec(\theta_0)$, depending on polarization (see Appendix B). The difference is more noticeable for 60° scan than it was for 30° scan.

For scanning in either of the principal planes, a grating lobe first appears at the

7

$$f_{GL} = \frac{f_0}{\sin(\theta_0) + 1} \qquad (1)$$

limiting the use of the array to frequencies less than f_{GL}. If a design objective is wide-angle scanning, it should be possible to improve the bandwidth performance by making the array lattice triangular instead of square. However, since such a structure is not self-complementary, its input impedance may be more frequency-dependent.

5. CONCLUSIONS AND RECOMMENDATIONS

This numerical investigation of the properties of planar bicone arrays has shown the extent to which they deviate from theoretical predictions of self-complementary arrays. The input impedance is fairly independent of frequency, with the real part remaining within 25% of $\eta_0/2$, except at frequencies near f_0 (the frequency at which the inter-element spacing is one wavelength). The detailed geometry of the feed region has only a minor effect on the input resistance, but a large effect on the input reactance. The useful bandwidth of the planar bicone array is not limited on the low end, but is limited on the high end by that frequency at which grating lobes begin to appear in visible space.

Further investigations are needed to establish the input impedance for triangular-lattice arrays, which should be capable of wider bandwidth for a given scan region. Also, directional elements, such as TEM horns need to be studied in order to design arrays that have unidirectional radiation, instead of the bidirectional radiation characteristic of planar bicones.

APPENDIX A - FINITE ELEMENT MODELING

A.1. Properties of Existing Computer Code

The calculations discussed in the body of this report used a computer code that was written to find transmissivity and reflectivity of generic periodic structures. It uses an expansion of the electric field inside the array unit cell in terms of linear "edge elements," volumetric functions defined over tetrahedral cells and referenced to the grid edges. These expansion functions have been repeatedly shown to yield accurate solutions for time-harmonic electric fields.

A sparse matrix S^I is constructed by first substituting the sum of edge element expansion functions with unknown complex scalar coefficients into the vector wave equation, and second, taking its inner product over the volume region (the unit cell) with the same functions (i.e. Galerkin's method). Next, the radiation boundary conditions at planes parallel to and outside the material structure are implemented by adding two matrices S^A and S^B, which have nonzero entries for each pair of edges in the lower and upper boundaries, respectively. The matrix terms are formed from inner products of the finite elements with a sum of Floquet modes. The addition of these matrices to S^I provides reflectionless boundaries that allows the mesh to be terminated arbitrarily close to the structure. Finally, periodicity conditions at unit cell side walls are implemented by mathematically folding opposite edges onto each other with a phase shift appropriate for the incident field's propagation angle. This folding can be written in terms of multiplication on the left by a matrix $\mathbf{R}$ and on the right by its Hermitian (conjugate transpose):

$$\mathbf{R}\left[\, S^A + S^I + S^B \,\right]\mathbf{R}^H \, \mathbf{E} \,=\, \mathbf{E}^{inc} \qquad\qquad (A1)$$

the incident field column vector $\mathbf{E}^{inc}$ is the inner product of the finite elements on one radiation boundary with the dominant Floquet mode.

The solution of the above matrix equation gives the vector of coefficients, $\mathbf{E}$, representing the electric field values along each edge of the mesh. The reflectivity and transmissivity are then found from those values on the radiation boundaries.

The existing code was valid for any combination of linear, isotropic dielectrics and perfect conductors. To perform the study of ultrawideband antennas, it was necessary to add

9

modifications for impedance loads, as described in the next section.

A.2. Resistive Wire Modifications

Representing a resistive wire in edge-based FEM is straightforward, provided that the wire coincides with grid edges (which is assumed to be the case). First, the matrix $\mathbf{S}^I$ is assembled as if the wire were not present. Then the diagonal entries corresponding to edges on each wire are modified as follows [8:325]:

$$\mathbf{S}'_{ii} = \mathbf{S}_{ii} + jk_0\eta_0\frac{L_i}{\rho_i} \tag{A2}$$

where L_i is the edge length and ρ_i is the wire resistivity (usually the same for all segments along a particular wire, regardless of whether the segments are the same length).

From the field solution, the potential across a wire segment is $V_i = e_i L_i$. Since the segment resistance is $R_i = \rho_i L_i$, the current through the wire is $I_i = e_i / \rho_i$.

It is important to preserve the conservation of power check within the code by accounting for that absorber by the resistive wires. The power absorber by a resistive wire segment is

$$P_i = I_s^2 \rho_i L_i \tag{A3}$$

The electric field strength incident on the radiation boundary is $|E^{inc}| = (A_{uc})^{-1/2}$, where A_{uc} is the unit cell area. The incident magnetic field strength is

$$| H^{inc} | = Y_{q00} A_{uc}^{-1/2}$$

where Y_{q00} is the modal admittance of the incident field mode, with $q=1$ for TE or 2 for TM:

$$Y_{100} = \frac{\cos\theta_0}{\eta_0} \tag{A5}$$

$$Y_{200} = \frac{\sec\theta_0}{\eta_0} \tag{A6}$$

10

where θ_0 is the angle of the incident wave measured from the array's surface normal. Finally, the incident power density is

$$p^{inc} = \frac{1}{\eta A_{uc}} \begin{cases} \cos\theta_0 & \text{TE} \\ \sec\theta_0 & \text{TM} \end{cases} \tag{A7}$$

and the total incident power is

$$P^{inc} = p^{inc} A_{uc} = Y_{q00} \tag{A8}$$

Hence, the power absorbed in a resistive segment is

$$P_i^{abs} = \frac{I_i^2 \, Y_{q00}}{R_i} \tag{A9}$$

APPENDIX B - FLOQUET MODE IMPEDANCES

Plane wave harmonics, or "Floquet modes," correspond to the lobes emitted by a transmitting array. The modes are evanescent for lobes that are not in visible space. For an array located in the $z=0$ plane with lattice spacings d_x and d_y and lattice skew angle γ, as shown in Figure B1, the modal impedances are [9:41-42]:

$$Z_{pmn} = \begin{cases} \dfrac{k\eta_0}{\kappa_{mn}} & TE\ (p=1) \\[4mm] \dfrac{\kappa_{mn}\eta_0}{k} & TM\ (p=2) \end{cases} \tag{B1}$$

$$\kappa_{mn} = \left[k^2 - k_{xmn}^2 - k_{ymn}^2\right]^{1/2} \tag{B2}$$

$$k_{xmn} = k\sin\theta_0\cos\phi_0 - \frac{2\pi m}{d_x} \tag{B3}$$

$$k_{ymn} = k\sin\theta_0\sin\phi_0 - \frac{2\pi n}{d_y} + \frac{2\pi m\cot\gamma}{d_x} \tag{B4}$$

where (θ_0,ϕ_0) is the scan angle (for transmit) or the incident wave angle (for receive). The modes are TE or TM to z.

In the case when only to the dominant ($m=n=0$) mode propagates, $\kappa_{mn} = k_0\cos(\theta_0)$ and the modal impedance reduces to

$$Z_{p00} = \begin{cases} \eta_0\sec\theta_0 & (p=1) \\[2mm] \eta_0\cos\theta_0 & (p=2) \end{cases} \tag{B5}$$

A planar bicone array, which radiates equally in both directions, will see an input impedance of $Z_{p00}/2$. Then a transmitting source with $\eta_0/2$ characteristic impedance will see a reflection coefficient of

12

$$R = \frac{\pm \sin^2\theta_0}{(1 + \cos\theta_0)^2}$$ (B6)

(positive for TM, negative for TE).

In the case of a square lattice with $d_x = d_y = \lambda_0$ and $\gamma = \pi/2$; with elements phased to radiate in the broadside direction, the propagation constant for the m,n mode is

$$\kappa_{mn} = \left[k^2 - \left(\frac{2\pi m}{d_x} \right)^2 - \left(\frac{2\pi m}{d_x} \right)^2 \right]^{1/2}$$ (B7)

or

$$\kappa_{mn} = k \left[1 - m^2 \left(\frac{f_0}{f} \right)^2 - n^2 \left(\frac{f_0}{f} \right)^2 \right]^{1/2}$$ (B8)

For frequencies below f_0, only the (0,0) mode propagates and there are no grating lobes. In the interval $f_0 < f < \sqrt{2}f_0$ the $(0,\pm 1)$ and $(\pm 1,0)$ modes can propagate. These modes correspond to grating lobes in the $\phi = \pi/2$, π, and $3\pi/2$ planes at

$$\theta_{GL} = \pm \sin^{-1}\left(\frac{f_0}{f} \right)$$ (B9)

Above $\sqrt{2}f_0$ another set of grating lobes forms in the diagonal planes. A transmitting source sees these higher order propagating modes as parallel impedances, although the impedance that each one presents depends on how well it couples to the currents on the antenna.

REFERENCES

1. Baum, Carl E. and Everett G. Farr, "Impulse Radiating Antennas," Ultra-Wideband, Short-Pulse Electromagnetics, ed. H.L. Bertoni, pp. 139-147, Plenum Press, 1993.

2. Giri, David V., "Radiated Spectra of Impulse Radiating Antennas (IRAs)," Sensor and Simulation Note #386, Nov. 1995.

3. Giri, David V. and Carl E. Baum, "Temporal and Spectral Radiation on Boresight of a Reflector Type of Impulse Radiating Antenna (IRA)," Ultra-Wideband, Short-Pulse Electromagnetics 3, ed. C.E. Baum, L. Carin and A.P. Stone, Plenum Press, 1997.

4. Buttram, Malcolm, "Introduction: Potential Applications in Government and Industry," Chapter 1 of High Power Optically-Activated Solid-State Switches, ed. A. Rosen and F. Zutavern, Artech House, 1994.

5. Deschamps, Georges A., "Impedance Properties of Complementary Multiterminal Planar Structures," IRE Trans. Antennas Propagat., pp. S371-S378, Dec. 1959.

6. Baum, Carl E., "Early Time Performance at Large Distances of Periodic Planar Arrays of Planar Bicones with Sources Triggered in a Plane-Wave Sequence," Sensor and Simulation Note #184, Aug. 1973.

7. McGrath, Daniel T., "Electromagnetic Analysis of Periodic Structure Reflection and Transmission by the Hybrid Finite Element Method," PL-TR-95-1103, USAF Phillips Laboratory, Sep. 1995.

8. Jin, Jian-Ming, The Finite Element Method in Electromagnetics, J. Wiley & Sons, 1993.

9. Amitay, Noach, Victor Galindo and Chen-Pang Wu, Theory and Analysis of Phased Array Antennas, Wiley-Interscience, 1972.
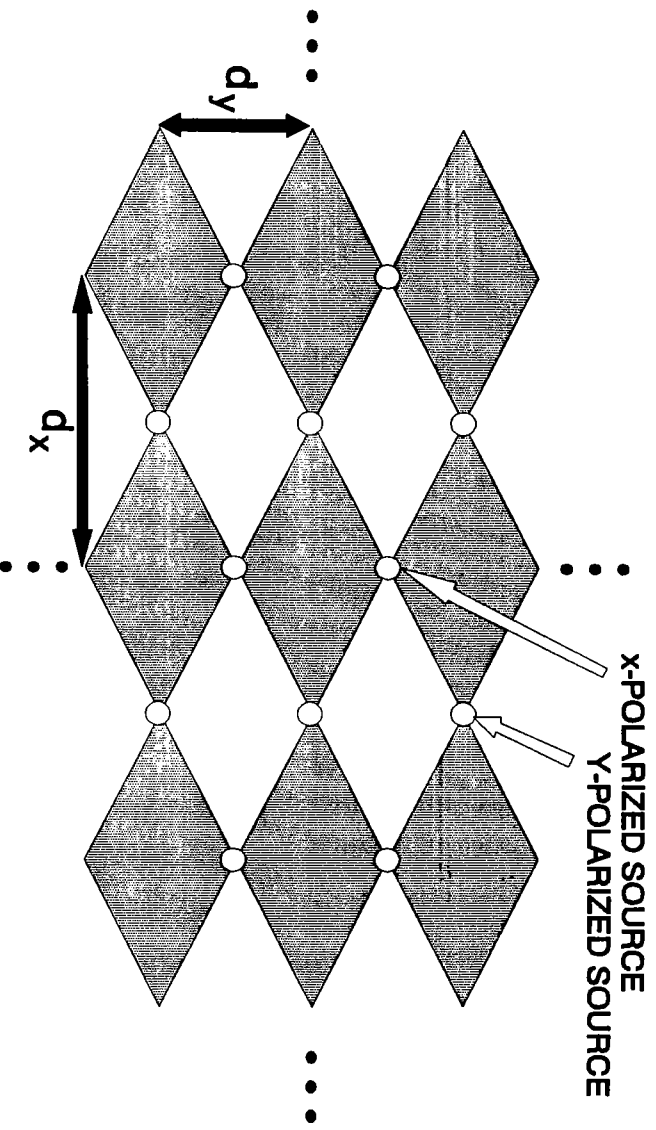
Figure 1. Planar Bicone Array

d_y

x-POLARIZED SOURCE
Y-POLARIZED SOURCE

d_x

CONDUCTING PLATES

SOURCES OR LOADS WITH
$Z_0/2$ IMPEDANCE
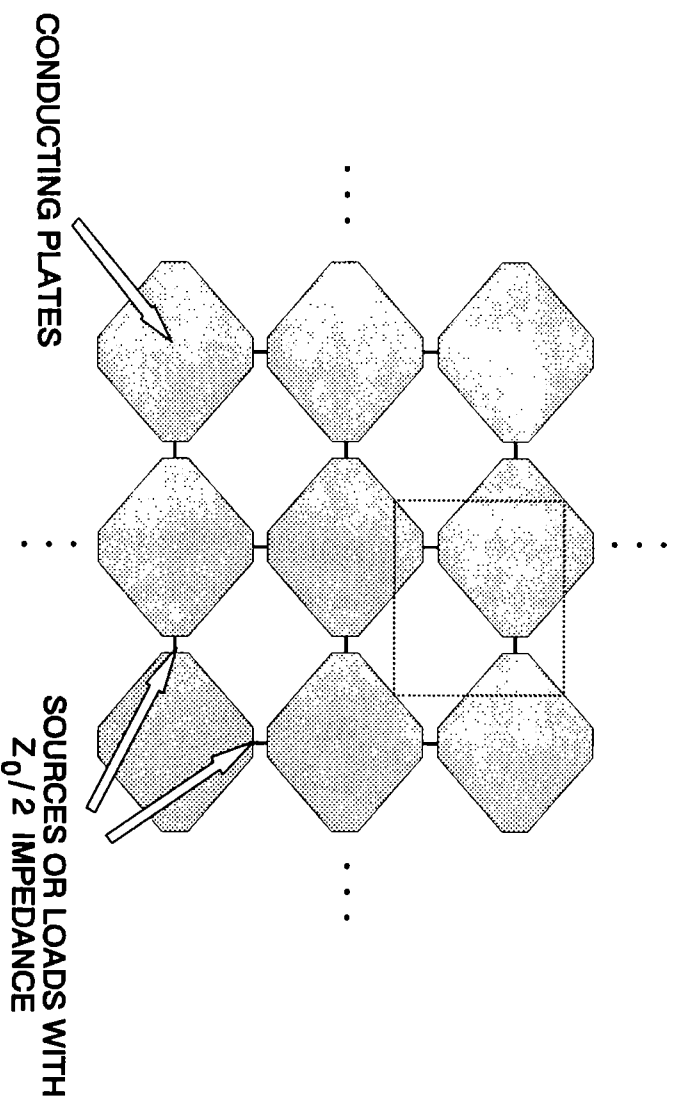
Figure 2. Planar Bicone Array with Unit Cell (dashed line)
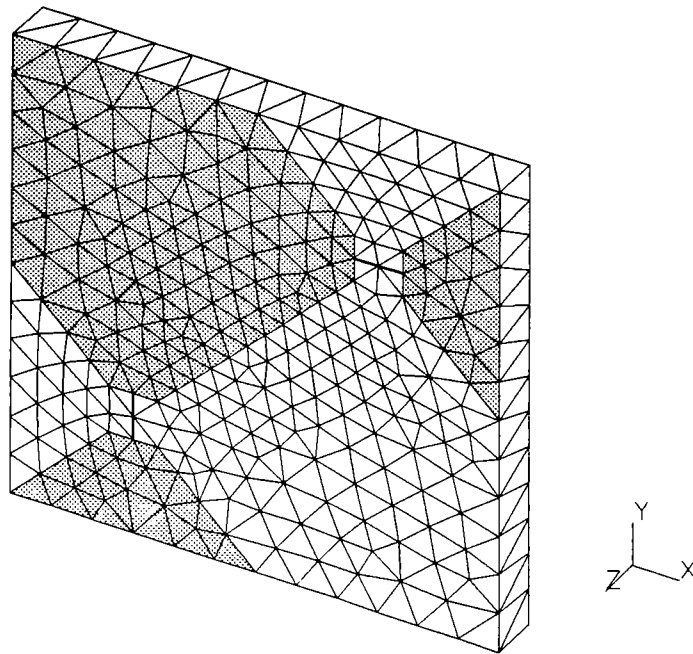
Figure 3. Subdivision of Unit Cell into Tetrahedra for Finite Element Analysis
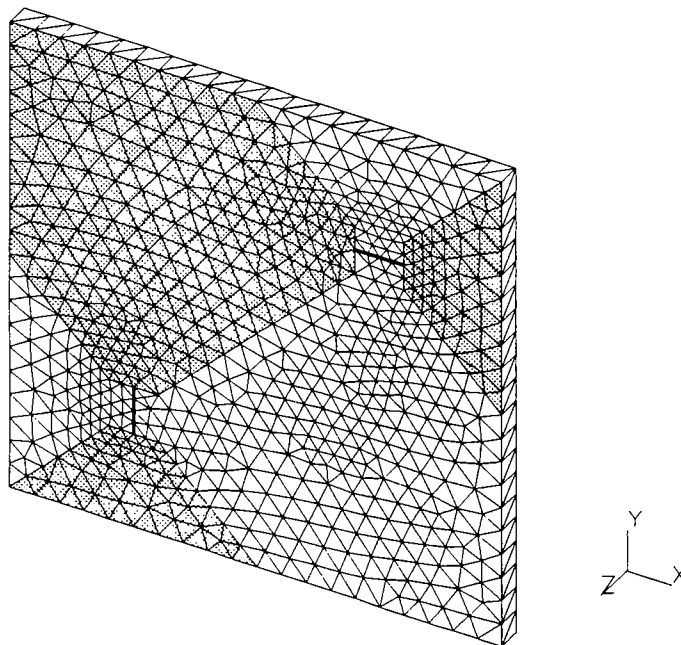(shading identifies conducting faces)

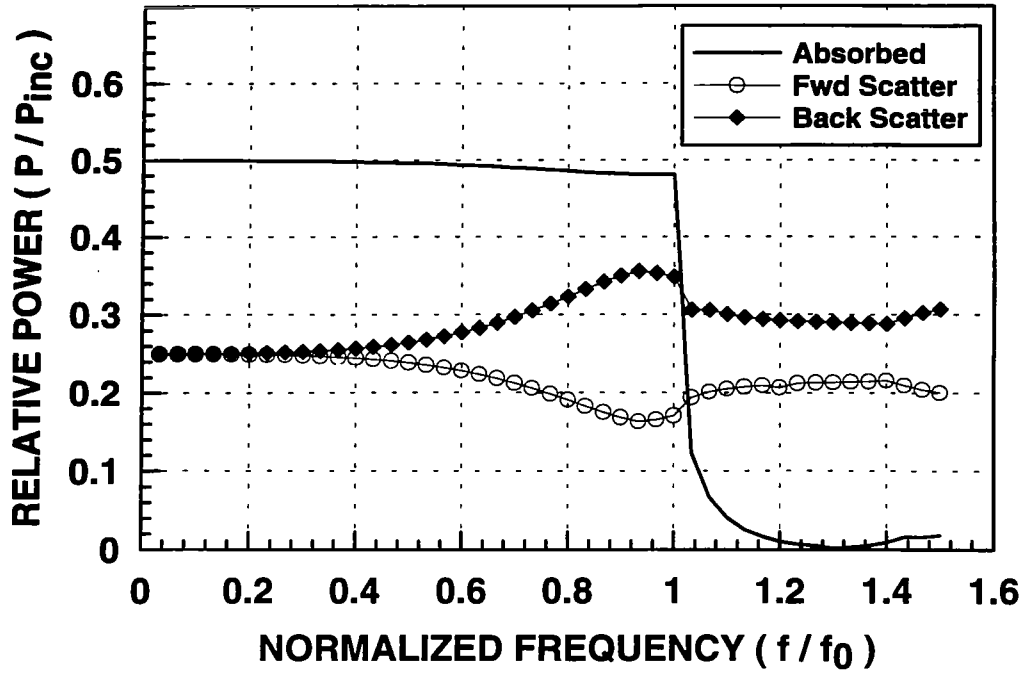Figure 4. Fine Resolution Grid used for Convergence Check

16

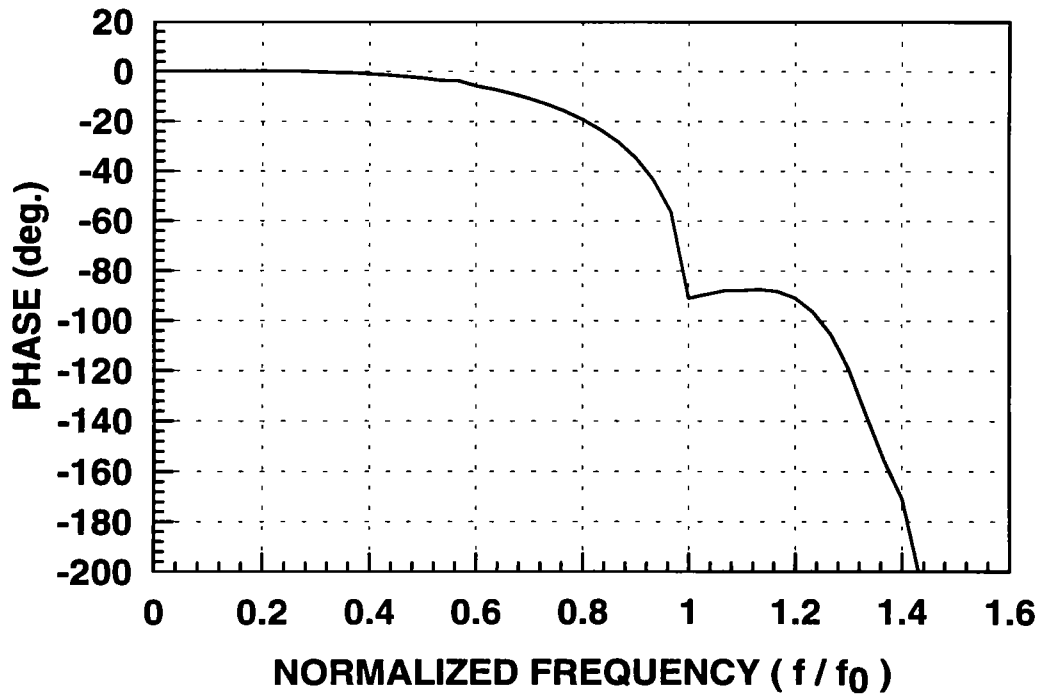Figure 5. Received and Scattered Power vs. Frequency, Broadside Incidence
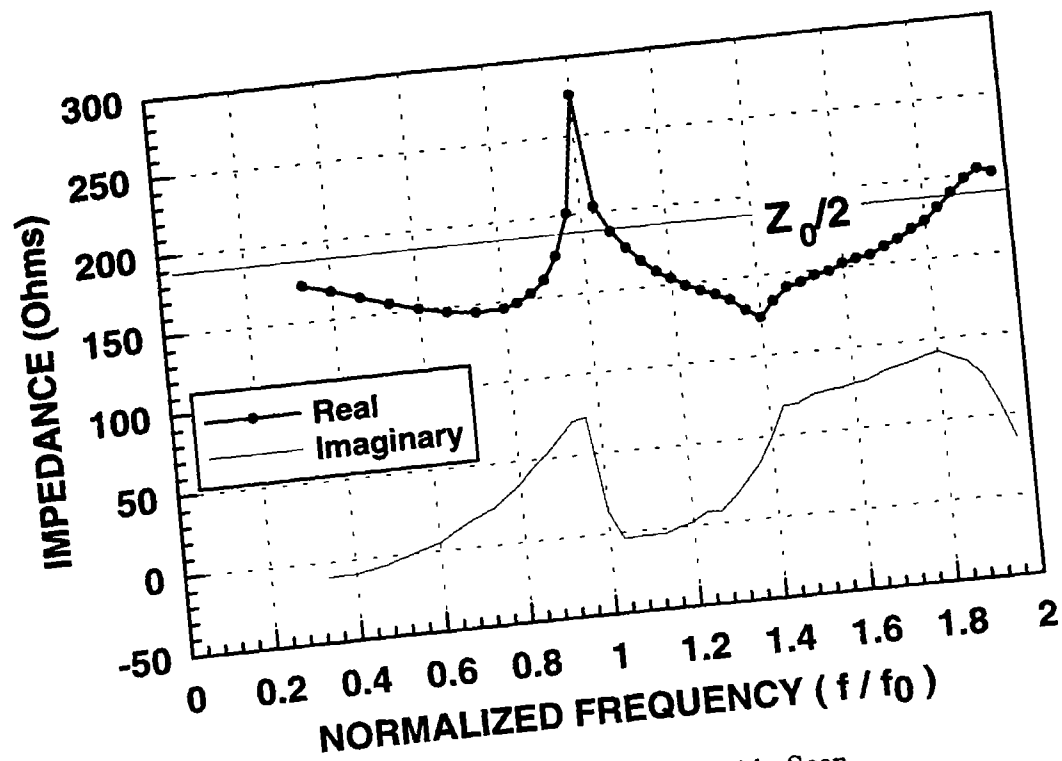

Figure 6. Received Phase, Broadside Incidence

17

Figure 7. Input Impedance, Broadside Scan
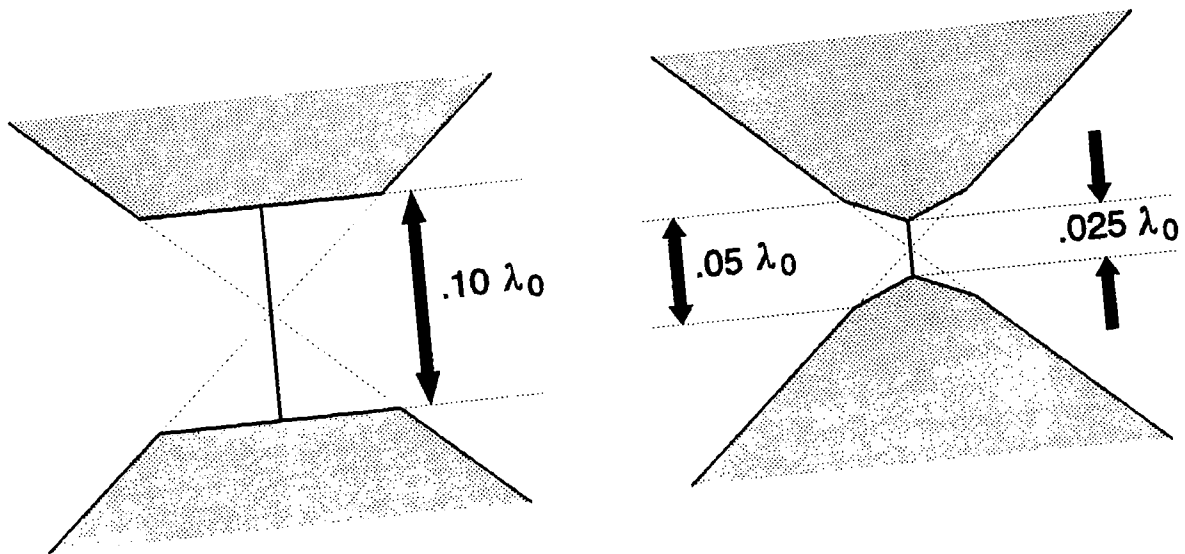
Figure 8. Alternative Feed Geometries: (a) Original, used for calculations in Figs. 5-7; (b) Refined
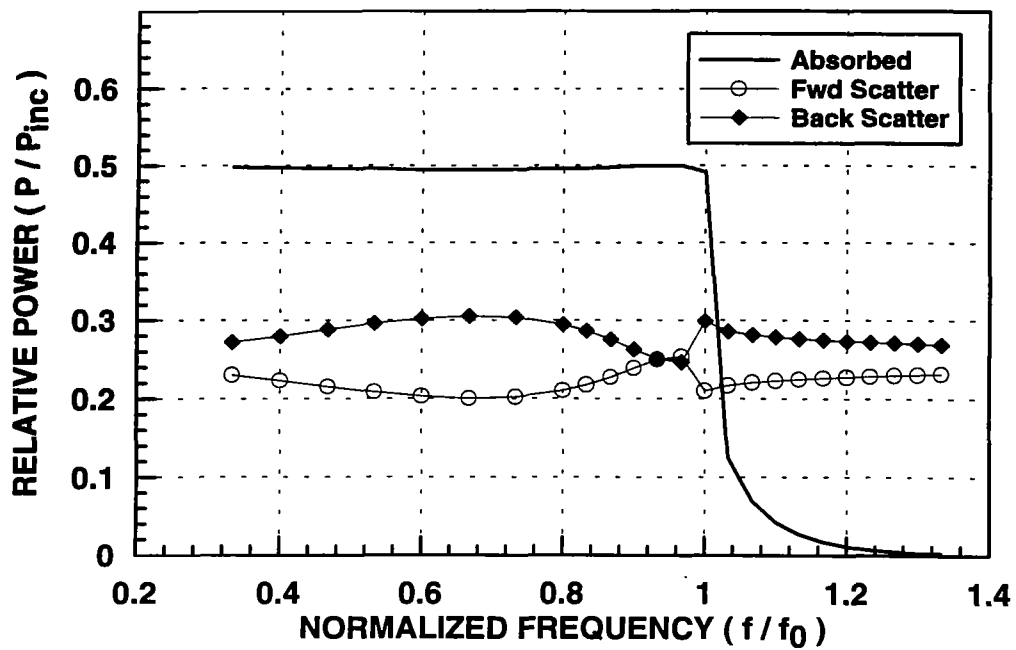
Figure 9. Received and Scattered Power for Refined Feed Geometry, Broadside Incidence
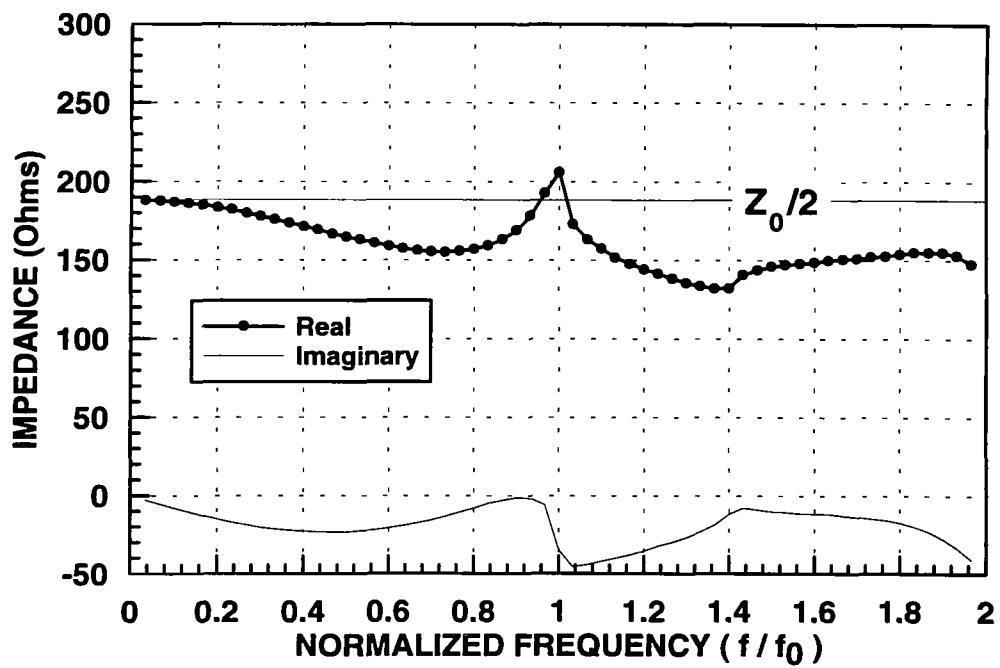
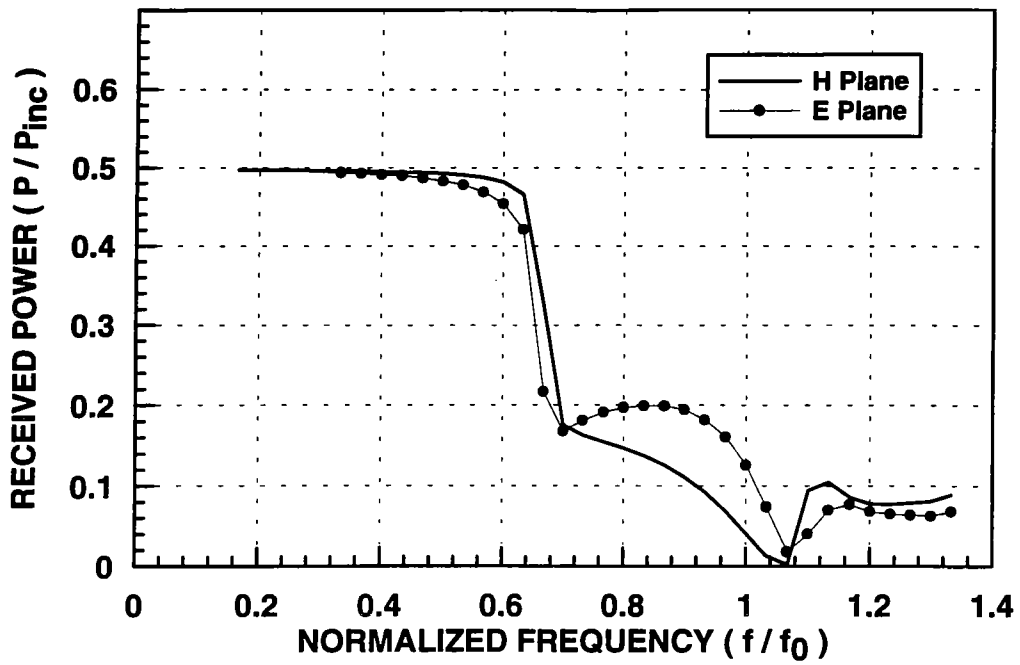Figure 10. Input Impedance with Refined Feed Geometry, Broadside Incidence

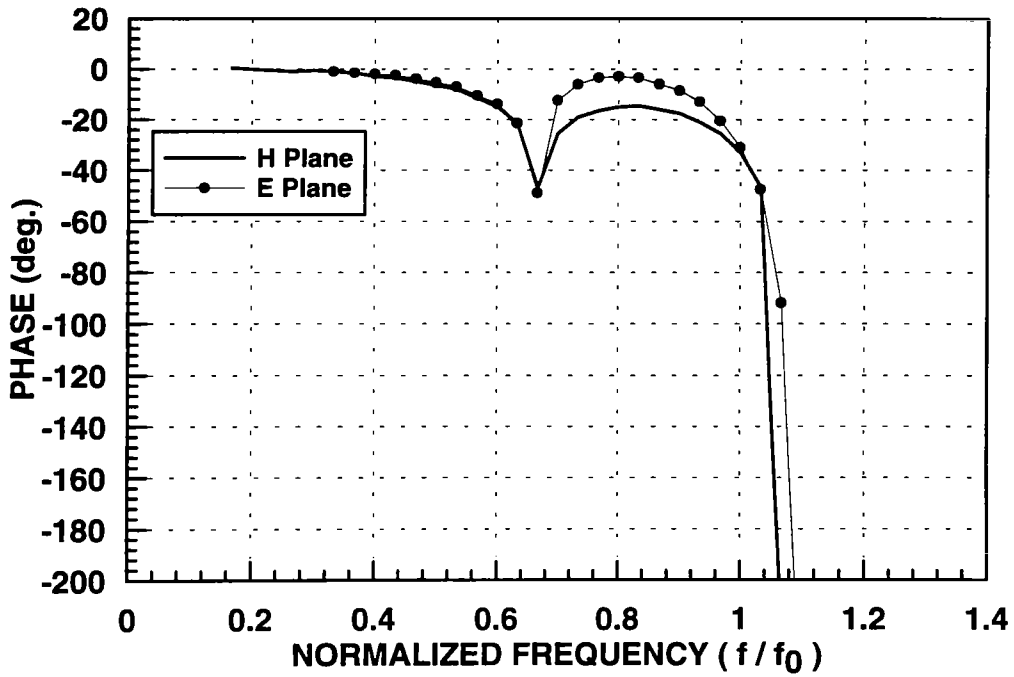Figure 11. Received Power vs. Frequency, 30° Incidence

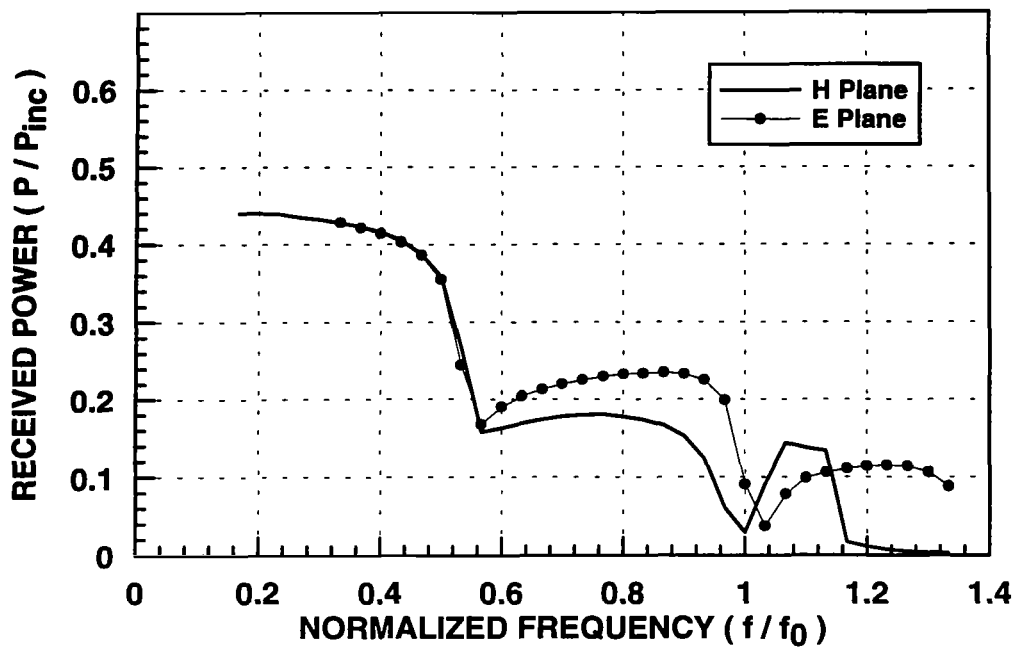Figure 12. Received Phase vs. Frequency for 30° Incidence

20

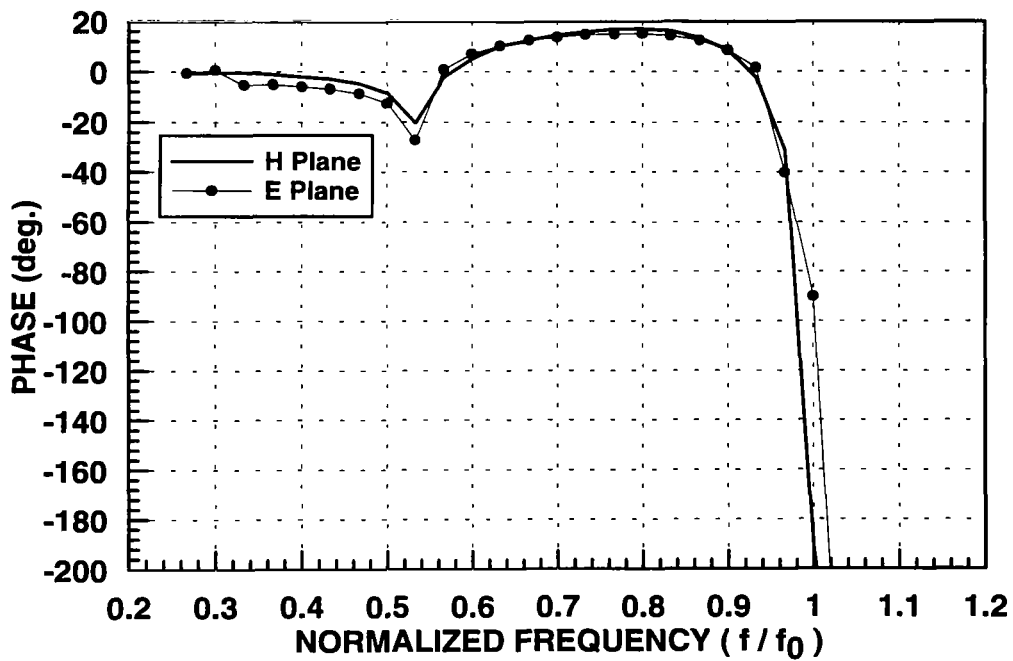Figure 13. Received Power vs. Frequency, 60° Incidence

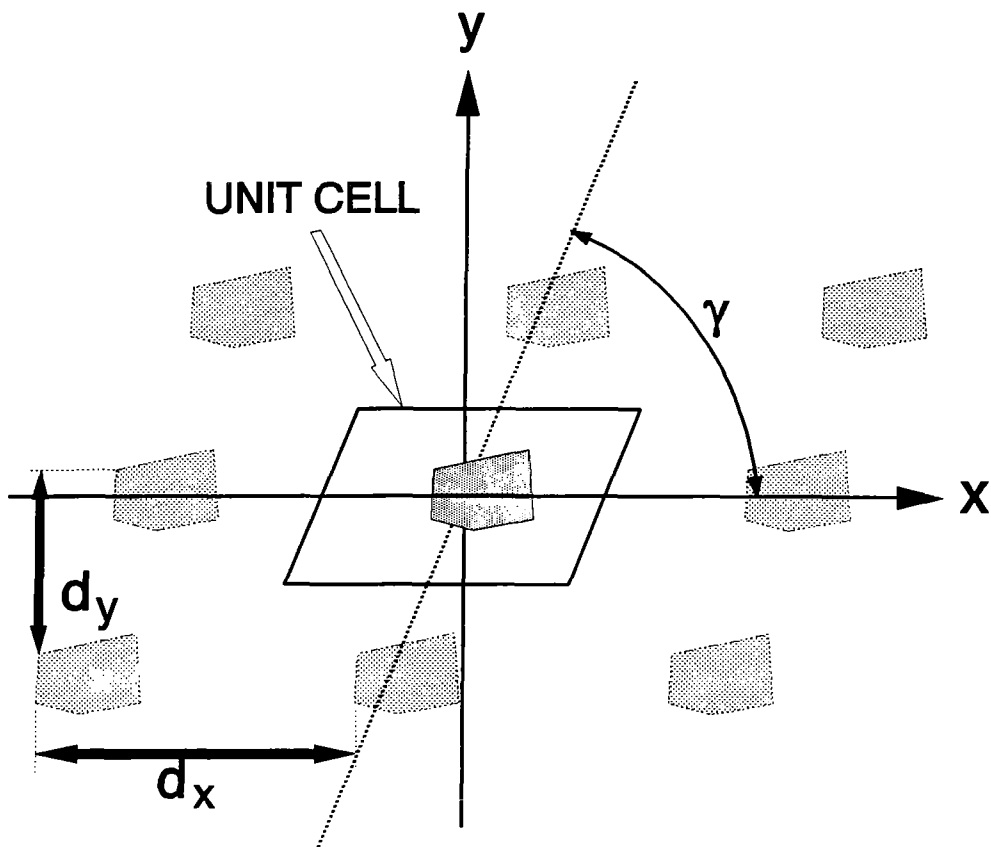Figure 14. Received Phase vs. Frequency for 60° Incidence

21

Figure B1. Generic Array Lattice Geometry

Table I. Convergence of Received Current vs. Number of Floquet Modes
(Table values are in mA)

	Low-resolution Grid		High-resolution Grid	
Modes	$.833\ \lambda_0$	$1.833\ \lambda_0$	$.833\ \lambda_0$	$1.833\ \lambda_0$
1	2.500	.8712	2.556	.7273
2	2.618	.7794	2.587	.7091
3	2.623	.7805	2.593	.7257
4	2.623	.7809	2.595	.7286
5	2.624	.7806	2.596	.7299
6	2.624	.7802	2.596	.7300
7	2.624	.7808	2.595	.7297
8	2.624	.7807	2.595	.7291
9	2.624	.7806	2.596	.7293
10	2.624	.7806	2.592	.7293
11			2.596	.7294
12			2.595	.7294
13			2.594	.7292